Food Structure 46 (2025) 100476

Contents lists available at ScienceDirect

Food Structure

journal homepage: www.elsevier.com/locate/foostr

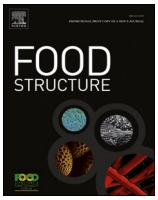

Rheology and crystallisation of cocoa butter in the presence of pea protein

Megan Holdstock [a], Brent S. Murray [a,b,*], Paraskevi Paximada [a], Michael Rappolt [a], Isabel Celigueta Torres [c], Anwesha Sarkar [a,b]

[a] Food Colloids & Bioprocessing Group, School of Food Science & Nutrition, University of Leeds, LS2 9JT, UK
[b] National Alternative Protein Innovation Centre (NAPIC), UK
[c] Nestlé Product Technology Centre, York YO31 8FY, UK

ARTICLE INFO

Keywords:
Cocoa butter
Pea protein
Rheology
SAXS
Crystallisation
Solid fat content

ABSTRACT

The effects of pea protein isolate (PPI) particles on the crystallisation and rheological properties of cocoa butter (CB) were evaluated. PPI particles were milled to produce two size classes, coarse and fine. Milled PPI particles were found to aggregate in molten CB, increasing the viscosity of the system and forming an elastic network. Greater aggregation was observed as the size of PPI particles was reduced. PPI particles had no effect on the crystal structure of CB, or the polymorphic transition pathway. However, the induction time of crystallisation was shorter, and the crystalline domain size in the α-phase was smaller for CB crystals + PPI, indicating heterogeneous nucleation effects. PPI particles increased the elasticity of the system by an order of magnitude only during the early stages of CB crystallisation. This study demonstrates that PPI particles can be incorporated into fat-based systems without disrupting fat crystal structure, with the potential to enhance mechanical strength. This highlights their potential as functional rheological modifiers upon milling in confectionery applications.

1. Introduction

Fats are utilised in a range of food, cosmetic and pharmaceutical products. Cocoa butter (CB) is of particular interest as a main component of chocolate and other confectionary systems. CB exhibits unique crystallisation behaviour, forming six crystal polymorphs with different mechanical and thermal properties. Solid particles are also key components in confectionery manufacturing and can affect key processing parameters, including the flow and crystallisation behaviour. Particles are typically embedded in a fat matrix, which nucleates upon cooling to form crystals which grow and aggregate into flocs to create a 3-dimensional fat crystal network (Co & Marangoni, 2019; Marangoni & Rousseau, 1996). The texture and melting attributes of confectionery systems like chocolate are dependent on the structural properties of this network, as well as the embedded particles (Beckett, 2009). Particle size distribution, crystallisation kinetics, and crystal structure significantly influence the macroscopic characteristics of such systems (Feichtinger et al., 2020; Kalic et al., 2018; Shewan et al., 2021; Yoshikawa et al., 2016).

Previous literature has predominantly focused on the effect of common chocolate ingredients, sugar and cocoa particles, on the properties of confectionery fats and their interactions with emulsifiers. The introduction of particle surfaces has been demonstrated to promote fat crystallisation, with this behaviour attributed to heterogeneous nucleation. In this mechanism the particle surface provides a site for triacylglycerol nucleation, lowering the free energy required (Metin & Hartel, 2005). Svanberg et al. reported that both sugar and cocoa particles accelerated crystal growth in non-seeded CB samples (Svanberg et al., 2011). Sugar has also been shown to influence fat crystal morphology, producing smaller, finer crystals which form a network with higher elasticity (10^6 Pa) than that of pure palm oil (10^5 Pa) (Hubbes et al., 2020; West & Rousseau, 2017).

In addition, the role of inorganic particles on fat crystallisation has been explored, including talc, carbon nanotubes and silica particles (Bayés-García et al., 2022; Chauhan et al., 2017; Yoshikawa et al., 2014, 2016). Yoshikawa et al. reported that the introduction of 1 % dispersed solid particles accelerated the crystallisation of CB, with polarised light microscopy revealing crystallisation on the surface of particles (Yoshikawa et al., 2014). Further work by the authors demonstrated that the addition of talc particles to palm-oil based shortening resulted in a denser, finer-meshed fat crystal network, like that of sugar/fat blends (Yoshikawa et al., 2016).

Comparatively little is known about fat crystallisation and flow behaviour in the presence of plant protein particles despite their

* Corresponding author at: Food Colloids & Bioprocessing Group, School of Food Science & Nutrition, University of Leeds, LS2 9JT, UK.
E-mail address: b.s.murray@leeds.ac.uk (B.S. Murray).

https://doi.org/10.1016/j.foostr.2025.100476
Received 27 August 2025; Received in revised form 29 September 2025; Accepted 2 October 2025
Available online 3 October 2025

increasing adoption in new food products. Recent work has explored techniques to use protein particles to formulate oleogel systems. However, these studies primarily involve a liquid oil phase, and so there is limited understanding on the effect of such particles on fat crystallisation. In addition, these oleogel systems have been formulated using indirect approaches involving numerous steps, starting with an aqueous dispersion of proteins to create emulsions, foams and hydrogels which undergo a drying or solvent exchange process to produce an oil continuous system (De Vries et al., 2015; Feichtinger et al., 2022; Romoscanu & Mezzenga, 2006; Sarkar et al., 2016), that may limit their application in industry.

Our previous work found that large, unmodified pea protein isolate (PPI) particles could be reduced to submicron sizes in liquid oil by stirred media milling (SMM). Milled PPI particles formed shear thinning aggregates in sunflower oil but at sufficient concentration form gel networks, that are stronger for smaller PPI particles (Holdstock et al., 2025). Such particles are still aggregates of numerous protein molecules, but it can be assumed that their outer surface reflects the complex distribution of hydrophilic and hydrophobic regions of their constituent individual proteins. However, how such milled plant protein particles affect the material performance of CB has not been explored in literature yet.

The present study explores the effects of the same insoluble plant protein particles on the rheology and crystallisation behaviour of CB. The structure and behaviour of these systems was characterised via rheology, microscopy and light scattering techniques for measurement of particle size. SMM was used to generate two sizes of protein particles: 'coarse' and 'fine' with average sizes of 17–18 and 1–3 μm respectively. The isothermal crystallisation behaviour of particle blends was characterised using pulsed NMR, small- and wide-angle X-ray scattering (SAXS/WAXS) and oscillatory shear rheology. To our knowledge, this work is the first study exploring the behaviour of pea protein particles in CB, demonstrating their potential to act as rheology modifiers.

2. Materials and methods

2.1. Materials

Pea protein isolate (PPI, Nutralys S85F, 83.8 % protein) was supplied by Roquette (Lestrem, France) and used as received in particulate form. Magnesium chloride salt was obtained from Sigma-Aldrich (Gillingham, UK). PPI particles were placed in a desiccator over a magnesium chloride saturated salt solution and equilibrated to room temperature for at least 5 days before use. This salt solution created an environment with a controlled relative humidity of 33 %. West African CB was provided by Nestle PTC (York, UK) and used without additional refining. Akomed-R MCT oil was obtained from AAK (Karlshamn, Sweden).

All data plotting and curve fitting throughout were performed using OriginPro 2024b (OriginLab, Massachusetts, USA). Samples were measured in triplicate and the mean values are presented with the standard deviations about these means shown as the error bars.

2.2. Preparation of protein suspensions via SMM

A stainless-steel grinding chamber (of volume 365 mL excluding spindle) plus a ceramic spindle were fabricated for use with a Silverson high shear mixer (L5M-A, Silverson, Chesham, UK). The mill was operated with a 0.5 grinding media to fill ratio, using yttrium-stabilised zirconium oxide milling beads of 600–800 μm diameter, plus usually 92 mL of molten protein particle suspension (~ 50 °C). After 1 min at 100 rpm, to allow the suspension to coat the milling beads, 4000 rpm was applied for 60–240 min in 15 min stages, with 5 min breaks in between, plus ice around the milling chamber to reduce heating. One set of fine particles had an average size of 1 μm, used in SAXS/WAXS experiments, and another set 3 μm for the other analyses. The former was obtained with a slightly lower fill volume (75 mL), while all other conditions were identical, but both these samples are considered comparable for the purposes of this study.

2.3. Particle size analysis

The particle size distributions (PSDs) of PPI particles were measured by light scattering with a Mastersizer 3000 equipped with the Hydro SM wet sample dispersion unit (Malvern Instruments, Worcestershire, UK). Suspensions were dispersed in sunflower oil until the laser obscuration exceeded 1 %. The refractive indices set to 1.464 for sunflower oil, and 1.54 for PPI particles in oil. The volume weighted mean diameter ($D_{4,3}$) was calculated in the usual way:

$$D_{4,3} = \frac{\sum n_i D_i^4}{\sum n_i D_i^3} \quad (1)$$

where n_i is the number of particles of diameter D_i.

For each sample, three replicates were measured, with five measurements taken per replicate; the reported values are the average of these measurements.

2.4. Rheology

Rheological characterisation of the PPI suspensions was performed using an Anton Paar MCR 302 rheometer (Anton Paar GmbH, Graz, Austria) at 50 °C. All measurements were conducted using a 50 mm diameter circular plate−plate geometry, sandblasted to avoid slip (upper plate PP50/S, lower plate Inset I-PP50/SS/S). Viscosity (η) was measured in the shear rate ($\dot{\gamma}$) range 0.01 −1000 s^{-1}. In amplitude sweep measurements the shear strain (γ) was varied logarithmically from 0.01 to 100 %, at 1 Hz. Oscillatory measurements were also conducted during crystallisation − samples were first heated to 80 °C, equilibrated for 10 min, then cooled to 20 °C at 3 °C min^{-1}. At 20 °C measurements were then performed every minute at 1 Hz and a low strain amplitude of 0.01 % to ensure measurements were within the linear viscoelastic region and to minimize shear disturbance on the crystallisation process. Measurements were performed in triplicate using a new sample loading and the mean values are presented in all rheology figures with the standard deviations about these means shown as the error bars.

2.5. Microscopy

Confocal microscopy (Leica DM6000 CS, Leica Microsystems, Wetzlar, Germany) was used to image PPI particles suspended in molten CB. The particles were stained with Fast Green (0.2 mg mL^{-1} in ethanol) which was gently mixed into the sample manually before placement on the microscope slide. Fluorescent imaging was performed using 633 nm laser excitation. Samples were subjected on a Linkam hot stage (LTSE 120, Linkam Scientific, Tamworth, UK) to the same thermal protocol as that described in Section 2.4 and crystallisation monitored for 15 min. Images were captured at 20x magnification and processed using ImageJ. A softening filter was also applied to reduce noise. These adjustments were made consistently across all images to improve visual clarity without altering the underlying data.

CB crystals formed during crystallisation were observed using polarised light microscopy (PLM) with a Leica DMLP microscope (Leica Microsystems, Wetzlar, Germany) equipped with the same model Linkam hot stage. A Nikon Camera (D3500, Nikon, Nishioi, Japan) was used to take images during variable intervals during isothermal crystallisation. Crystal morphology was visualised using 20x and 50x objective lenses.

One drop of molten sample (at 50 °C) was placed on a glass microscope slide and covered with a square coverslip. Samples were subjected on the Linkam stage to the same thermal protocol to that described in Section 2.4 and crystallisation monitored for 1 h with images taken

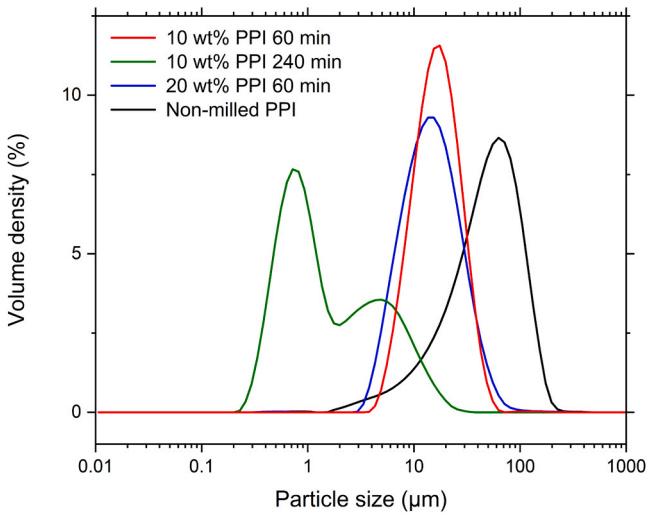

Fig. 1. Particle size distributions for non-milled and milled PPI in molten CB. Non-milled (black), 10 wt% milled for 60 min (red), 20 wt% milled for 60 min (blue), 10 wt% milled for 240 min (green).

every 10 min. The samples were then transferred to a temperature-controlled lab at 20 °C and imaged at various time intervals. Bright-field microscopy images were also taken using the same apparatus.

2.6. X-ray scattering

SAXS/WAXS experiments were performed using a SAXSpace instrument (Anton Paar GmbH, Graz, Austria). The instrument is equipped with a Cu anode and operates at 40 kV and 50 mA ($\lambda = 0.154$ nm) with a temperature-controlled stage (± 0.1 °C). Simultaneous SAXS/WAXS measurements were performed at a sample-detector distance of 130 mm, covering a scattering vector q range from 0.1 to 17.6 nm^{-1} where $q = 4\pi(\sin\theta)/\lambda$, with 2θ being the scattering angle. The 1D scattering patterns were recorded with a Mythen microstrip X-ray detector (Dectric Ltd., Baden, Switzerland). Melted samples were injected into 1.5 mm quartz disposable capillaries (Capillary Tube Supplies Ltd., Cornwall, UK) then sealed with wax.

SAXS/WAXS measurements were carried out following a similar heating protocol to that used for rheological and PLM measurements. Samples were first equilibrated at 20 °C for 5 min, then heated to 80 °C at a constant rate of 3 °C min^{-1}. Upon reaching 80 °C, the samples were equilibrated for 10 min to completely melt and erase any crystal memory. This was followed by cooling at 3 °C min^{-1} to 20 °C. Measurements were then performed continuously for 10 min with an exposure time of 1 min, followed by every 10 min for 120 min, every 30 min for 24 h and after 2, 3, 4, 7, 10, 16, 21, and 28 days.

The position of the primary beam of all scattering patterns was set to zero using SAXStreat software (Anton Paar GmbH, Graz, Austria). All data were then normalised for their transmission using SAXSquant software (Anton Paar GmbH, Graz, Austria), setting the scattering intensity at $q = 0$ to unity. The normalised empty capillary scattering was then subtracted from the normalised sample patterns. It must be noted that resulting diffraction patterns contained smeared peaks due to the line-focus collimation system. For identification of the polymorphs and TAG chain packing and stacking distances, no de-smearing procedure was required. The tilt angle of the hydrocarbon chains in the 2L-stackings of TAGs was estimated via a geometrical approach detailed by Pratama et al. (2022) (note, a crystallographically-refined value for the extension of the glycerol backbone of 2.54 Å was used), estimating the

Table 1
Mean $D_{4,3}$ values (± standard deviations) of non-milled and milled PPI particles in CB at time intervals up to 240 min at 4000 rpm stirrer speed and particle concentrations of 10 wt % and 20 wt%. Different lower-case letters in the same column indicate a statistically significant difference ($p < 0.05$).

Sample	$D_{4,3}$ (μm)
Non-milled PPI	57.0 ± 1.8^{a}
10 wt% PPI 60 min	18.3 ± 0.2^{b}
20 wt% PPI 60 min	17.4 ± 0.3^{b}
10 wt% PPI 240 min	2.9 ± 0.2^{c}

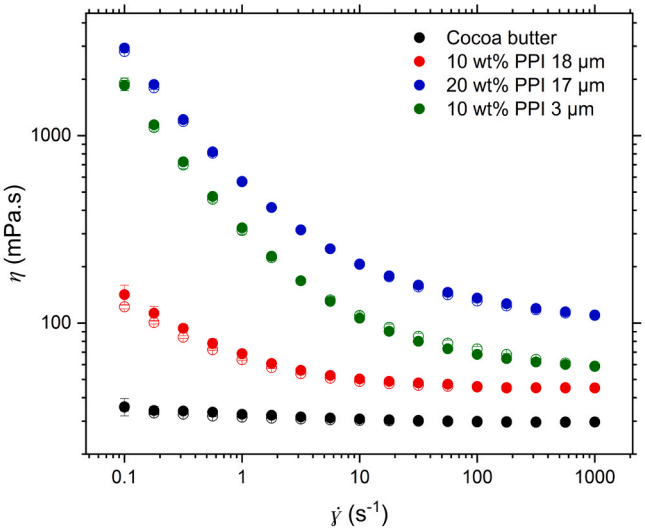

Fig. 3. Viscosity (η) of milled PPI in molten CB (at 50 °C) as a function of shear rate ($\dot{\gamma}$): CB (black), 10 wt% PPI 18 μm (red), 20 wt% PPI 17 μm (blue), and 10 wt% PPI 3 μm (green). Increasing $\dot{\gamma}$ sweeps are represented by the filled symbols, the reverse $\dot{\gamma}$ sweep is given by the unfilled symbols.

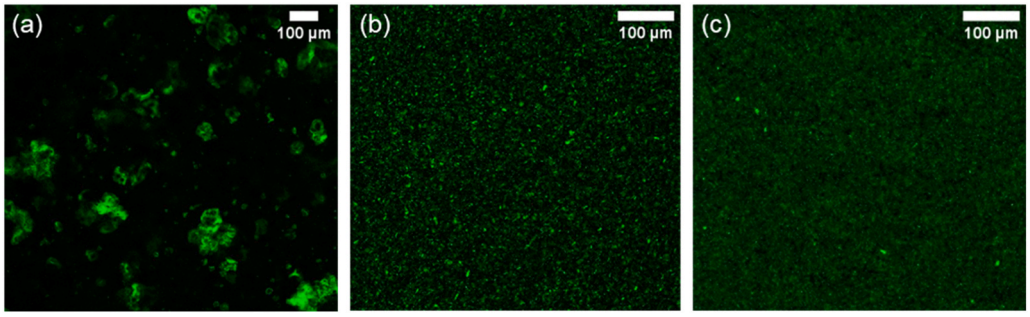

Fig. 2. CLSM images of 10 wt% PPI milled in CB for (a) 0 min, (b) 60 min, (c) 240 min at 80 °C. A softening filter in ImageJ was applied consistently across all images.

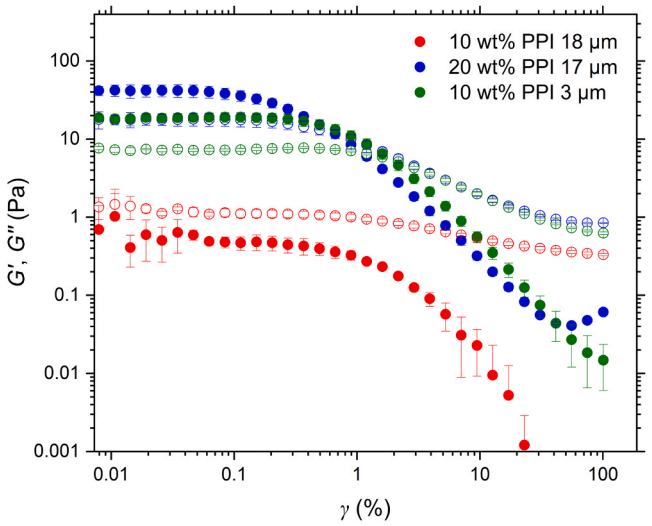

Fig. 4. Oscillatory shear strain (γ) sweeps of milled PPI dispersed in molten CB (at 50 °C): 10 wt% PPI 18 μm (red), 20 wt% PPI 17 μm (blue), and 10 wt% PPI 3 μm (green). *G'*: filled symbols. *G''*: open symbols.

average carbon chain length of CB as 17.5 Å, based on mass spectroscopy measurements reported by Simone et al. (2024).

The crystalline domain size (ξ) was determined from the SAXS patterns using the Scherrer equation:

$$\xi = \frac{K\lambda}{\beta_{sample}\cos(\theta)} \tag{2}$$

where K is the Scherrer constant, λ is the wavelength of the X-ray, θ is the diffraction angle and β_{sample} is the full width at half of the maximum (FWHM) of the (001) small-angle X-ray reflection peak after adjustment for instrumental broadening (see Eq. 3). A K value of 0.9 was used, as is typical for such systems (Acevedo & Marangoni, 2010).

The diffraction broadening is a convolution of both physical and instrumental broadening. To eliminate the effect of instrumental broadening on ξ, the measured FWHM was corrected. The intrinsic and instrumental profiles were approximated to Lorentzian and Gaussian functions, respectively. The attenuated direct beam profile is routinely recorded together with each SAXS pattern, which was used as the instrumental direct beam profile. We note that most instruments have a Gaussian shaped instrumental profile. The FWHM of each component were then described using the Lorentzian-Gaussian relationship (He et al., 2018; Zhang et al., 2003):

$$\frac{\beta_{sample}}{FWHM} = 1 - \left(\frac{\beta_{instrumental}}{FWHM}\right)^2 \tag{3}$$

where *FWHM*, β_{sample} and $\beta_{instrumental}$ are the FWHM values of the experimental, instrumental, and intrinsic profiles, respectively. It should be noted that the intrinsic diffraction peak is best fitted with a Lorentzian shape as crystallite size analysis was only applied to metastable polymorphs (α- and β'-phases).

2.7. Solid fat content (SFC) analysis

SFC measurements were performed using pulsed NMR (Minispec mq20, Bruker BioSpin, Rheinstetten, Germany) using the indirect method AOCS Cd 16–81. This method was used because the direct method (AOCS Cd 16b-93) would inflate the SFC by detecting solid (protein) particles alongside solid fat (Firestone, 1998; Simoes et al., 2021; West & Rousseau, 2016). The indirect method compares the free induction decays (FIDs) of the liquid-state protons from the sample and a fluid reference oil at the temperature of interest, i.e., 20 °C, and at 60 °C, where the fat is fully molten, to determine the SFC using equation:

$$SFC = \left(1 - \left(\frac{S20}{S60}.Q\right)\right).100 = \left(1 - \left(\frac{S20}{S60}.\frac{R60}{R20}\right)\right).100 \tag{4}$$

where S20 and S60 are the signal intensities of the sample at 20 and 60 °C, respectively. Akomed-R MCT oil was equilibrated at 20 (R20) or 60 °C (R60) and used as the reference oil, remaining fluid across the measurement range. The Q factor (R60/R20) corrects for the temperature dependence of the receiver sensitivity (Gribnau, 1992)

Glass NMR tubes were filled with 1.5 mL of sample and held at 60 °C for 10 min to equilibrate, before signal collection for the indirect method calculation. The samples were then transferred to an 80 °C heating block for 10 min. Following the X-ray protocol, the samples were then cooled down to 20 °C, held for 3 min to allow for temperature equilibration, then measurements made at variable intervals over 120 min. Due to the limited number of heating blocks present in the Minispec, it was not possible to generate a continuous cooling ramp as was used in the X-ray protocol. To accommodate this, a stepwise cooling approach was used. After thermal equilibration at 80 °C, samples were cooled sequentially to 65 °C and then 50 °C, holding for 5 min at each step. The samples were then cooled from down to 20 °C in 6 °C increments, being held in each block for 2 min. This stepwise cooling method corresponded to an average overall rate of 3 °C min^{-1}, as in the X-ray measurements. Samples were measured in triplicate and the mean values are presented with the standard deviations about these means shown as the error bars.

The crystallisation kinetics of the samples analysed by fitting the final isothermal plots of SFC vs time to the modified Gompertz equation for a two-step crystallisation process (Foubert et al., 2006):

$$SFC(t) = SFC_1.\left(1 - \exp\left(-\frac{2\mu_1}{SFC_1}.t\right)\right) + SFC_2.\exp\left(-\exp\left(\frac{\mu_2.e}{SFC_2}(l - t) + 1\right)\right) \tag{5}$$

where SFC_1 represents the amount of solid fat crystallised in the first step, μ_1 is the growth rate of the first step, SFC_2 denotes the SFC formed after the second step, μ_2 is the growth rate of the second step and l is the induction time of the second step.

All data plotting and curve fitting throughout were performed using OriginPro 2024b (OriginLab, Massachusetts, USA).

2.8. Data analysis

Statistical analysis on the significance between data sets was calculated using analysis of variance (ANOVA) with Tukey post hoc test, significance level $p < 0.05$.

3. Results and discussion

3.1. PPI particle size

Dry, non-milled PPI 'dispersed' in oil consists of large particles (Figs. 1 and 2a) that sediment rapidly, composed of aggregated proteins formed during the extraction process (Li et al., 2023). The presence of particles above 30 μm leads to poor mouthfeel in confectionery products (Beckett, 2009). Previous work showed that SMM in sunflower oil could reduce the mean size into the submicron region, with longer milling times increasing the population of PPI in this size range (Holdstock et al., 2025).

Milling 10 wt% PPI in CB for 60 min reduced $D_{4,3}$ from 57.0 μm to 18.3 μm and the PSD showed a monomodal peak (Fig. 1). After 240 min the PSD shifted to smaller sizes and became bimodal, indicating the presence of a submicron (0.01–1 μm) and a larger micron-sized

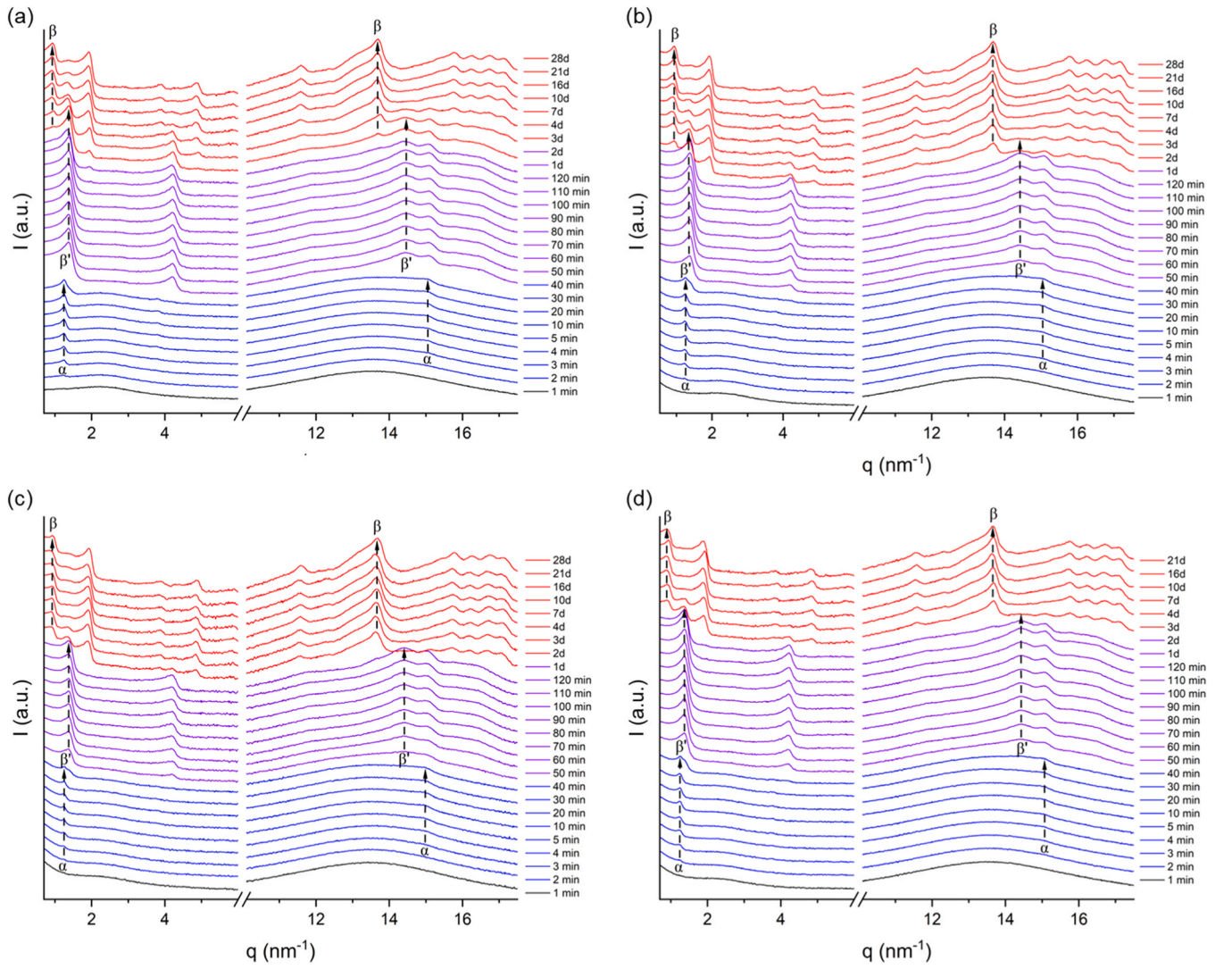

Fig. 5. Evolution of the CB structure at 20 °C of (a) CB and CB with (b) 10 wt% PPI 18 μm, (c) 10 wt% PPI 1 μm and (d) 20 wt% PPI 17 μm observed by small- and wide-angle X-ray scattering. The different phases are colour-coded as follows: fluid phase (black), α-phase (blue), β'-phase (magenta), and the β-phase (red). First-order reflections in the SAXS region and reflections in the WAXS region are indicated as identified. Enlarged versions of panels (a–d) are provided in the Supplementary Material as Figs. S3–S6 for clarity.

(1–30 μm) particle population, further reducing $D_{4,3}$ to 2.9 μm (Table 1). Milling at a higher solids concentration of 20 wt% (for 60 min) decreased $D_{4,3}$ to 17.4 μm, i.e., similar to that obtained at 10 wt%. Confocal microscopy (CLSM) confirmed the differences between the different milling times (Fig. 2). The 10 wt% system milled for longer time shows predominantly smaller particles but also a few larger particles or agglomerates (Fig. 2c), reflecting the bimodality of the PSD. The CLSM images of the larger PPI particle system appeared to be more homogenous in size (e.g., Fig. 2b), corresponding to the more unimodal PSD (Fig. 1). Similar PSDs were reported for milling PPI in sunflower oil earlier (Holdstock et al., 2025). After cooling from 80 °C to 20 °C no significant change in protein structure or size was observed, suggesting the high temperature has limited effect on the protein in cocoa butter (Figure S1).

3.2. Effect of PPI on molten CB rheology

3.2.1. Flow behaviour

Fig. 3 shows that, the milled PPI-CB suspensions exhibited non-Newtonian, shear-thinning behaviour. As the size of PPI particles was reduced from 18 μm to 3 μm, the low shear η of the system increased by an order of magnitude. This indicated structure formation due to particle aggregation, which becomes more significant as the particle size is reduced due increased surface area and reduced average distance between particles. At a PPI size of 17–18 μm, increasing solids from 10 to 20 wt% also increased η, due to the higher overall particle surface area and particle-particle interactions. At the same solids concentration, the high shear η of both sizes of PPI particles were similar, suggesting that any such structure was broken down by the mechanical forces exerted at the highest $\dot{\gamma}$ (i.e., 200–10^3 s^{-1}).

Fig. 3 shows measurements of η as $\dot{\gamma}$ was reduced back to the lowest value in the reverse sequence of steps. There was no significant hysteresis, indicating complete reversibility of any structural break down and agglomeration of particles, at least over this range of $\dot{\gamma}$ and time scales. This suggests that the forces driving aggregation between PPI particles in molten CB are relatively weak.

3.2.2. Dynamic rheology and gel formation

Fig. 4 shows that, for suspensions of the milled PPI particles with the larger size ($D_{4,3}$ ~ 18 μm), the material behaviour varied with solids content. At the lower solids concentration (10 wt%), we observed viscous behaviour, i.e., loss modulus (G'') > storage modulus (G').

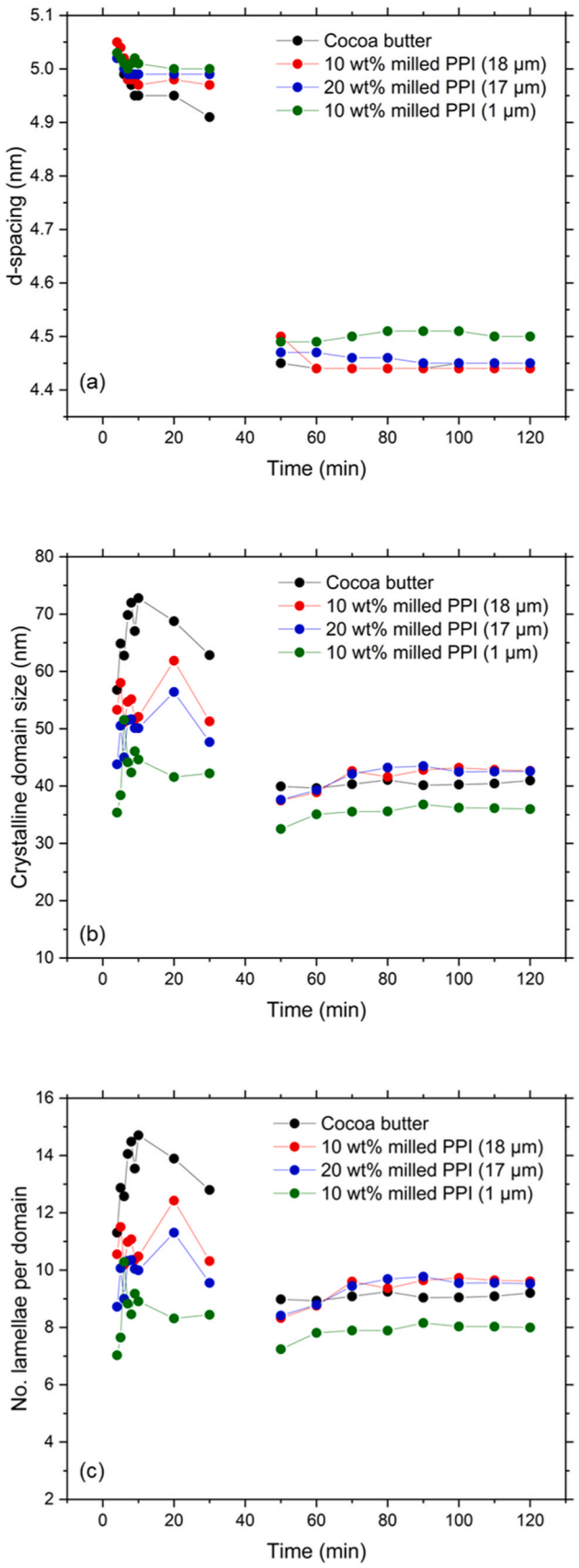

Fig. 6. (a) The d-spacing, (b) crystalline domain size, and (c) number of lamellae per domain, obtained using long spacing peak parameters (peak position and FWHM) of CB (black) and CB with 10 wt% PPI 18 μm (red), 20 wt% PPI 17 μm (blue), and 10 wt% PPI 1 μm (green), crystallised at 20 °C for 120 min.

Increasing the solids concentration to 20 wt% resulted in gel-like behaviour, shown by the plateau in both G' and G'', defining a linear viscoelastic region (LVER), but $G' > G''$. This suggests that, at 10 wt% the 18 μm PPI particles formed isolated structured aggregates which flow when perturbed but at 20 wt% the increased overall particle surface area and particle-particle interactions enabled the formation of an elastic network. The smaller PPI particles ($D_{4,3} \sim 3$ μm) exhibited a LVER where $G' > G''$ at only 10 wt%, due to more particle-particle interactions per unit mass (larger specific surface area), demonstrating that elasticity is achievable at this concentration with a six-fold size reduction. Increasing γ disrupts these networks, indicated by the moduli crossover, after which the response is dominated by G''.

Thus, the milled protein particles can act as structuring agents in CB in a similar fashion to other oleogel systems (de Vries et al., 2017; Feichtinger et al., 2022; Plazzotta et al., 2020). However, it should be noted that sedimentation occurred after several hours, (but on timescales far longer than those of rheological measurements).

Differences in the strain limit of the linearity (γ_0) were observed between the two gel-like suspensions. The 10 wt% 3 μm PPI exhibited a larger LVER ($\gamma_0 = 0.9$ %) compared to the 20 wt% 17 μm particles ($\gamma_0 = 0.2$ %). However, the larger particles formed networks with a higher elasticity ($G' \sim 18$ Pa) than the smaller particles ($G' \sim 7$ Pa). This suggests that the network formed by the smaller PPI is more effective at dissipating deformation, potentially due to increased mobility within the network compared to the larger particles. A similar relationship between γ_0 and particle size has been reported for milled PPI particles in sunflower oil (Holdstock et al., 2025).

3.3. Isothermal crystallisation behaviour

3.3.1. Effect of PPI particles on CB crystal structure

The temporal evolution of diffraction patterns for CB and CB with milled protein particles of varying size and concentration, crystallising statically under isothermal conditions, is shown in Fig. 5. Molten CB alone first crystallises into the α-form within the first couple of min after the isothermal target temperature has been reached. During the isothermal hold, a polymorphic transformation occurs, with the α-form transitioning to the more stable β'-IV form after 50 min, followed by the eventual formation of the β-V polymorph. The β-form appears after a couple of days under isothermal conditions. Importantly, the stepwise crystallisation pathway of CB appeared unchanged in the presence of the PPI, with identical polymorphic transitions observed. For all samples, the WAXS peaks developed alongside those in the SAXS region. However, some differences in the kinetics were observed. The first-order reflection of the β-polymorph in the SAXS region becomes prominent after 2 days for the 10 wt% PPI samples, whilst this occurs after 3 days for the pure CB and the 20 wt% PPI sample (Fig. 5). PPI also accelerates the development of the 5th-order SAXS reflection associated with the β-polymorph (Figure S2), evolving most rapidly in the 10 wt% PPI samples, followed by 20 wt% PPI, and slowest in CB. This suggests that PPI promotes the β' to β transition, but additional measurements over this period are required to confirm these observations.

Fig. 6a shows the time evolution of the lamellar repeat distances (d-spacing) of the α- and β'- polymorphs during the first 120 min. In pure CB, the d-spacing is reduced from 49.5 Å to 44.4 Å upon transformation to the β'-form, attributed to the tilting of the TAG molecules at an angle of 28°. The β-form has a d-spacing of 64.3 Å, increasing as the TAG molecules form a 3-L lamellar arrangement. These results are in good agreement with literature (Ladd Parada, 2018). The presence of PPI does not significantly affect the lamellar distances of the CB TAG molecules within the crystal (Fig. 6a). In the wide-angle regime, the peak positions were also unchanged, indicating comparable chain packing between the

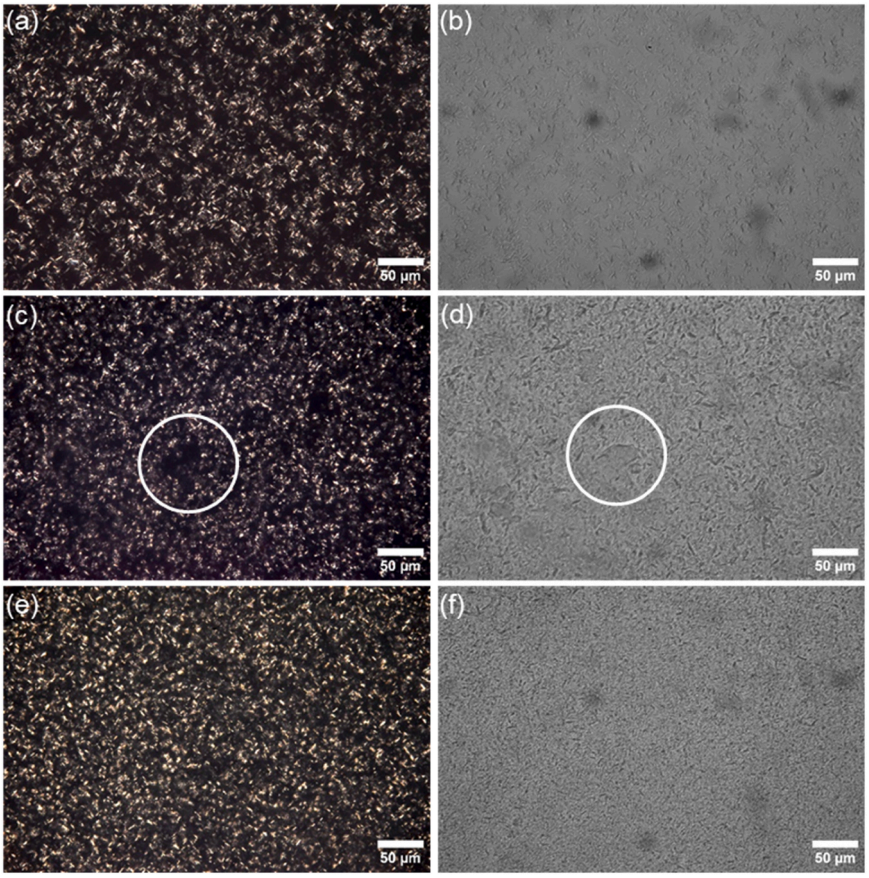

Fig. 7. PLM (a, c, e) and OM (b, d, f) images of (a, b) CB and CB with varying particle sizes of PPI at a concentration of 10 wt%, (c, d) 18 μm and (e, f) 3 μm after crystallisation at 20 °C for 20 min. Larger protein particles visible in (c) and (d) are highlighted by circles. All images were taken at 50x magnifcation and OM images were brightness adjusted to improve visibility.

different systems. This suggests that PPI is not integrated into the CB crystal lattice.

The crystalline domain size can be determined from broadening of the diffraction peaks using the Scherrer equation (Eq. 2). The domain size calculated by the Scherrer equation is the thickness perpendicular to the crystal plane and is an average of the material (He et al., 2018). In all systems, the crystalline domain size initially increases during the α-phase as the crystal nuclei grow (Fig. 6b). After 10 min, the domain size in pure CB significantly decreases as the crystallisation of the β'-phase begins. The d-spacing, crystalline domain size and thus number of lamellae per domain remain relatively constant from 50 to 120 min. [Data at 40 min have been omitted due to the coexistence of the α- and β'-phase first order peaks, leading to broadening of the superimposed diffraction peaks and reduced analysis reliability].

The presence of PPI reduces the crystalline domain size in the α-phase. After 20 min under isothermal conditions, the CB blend with the smaller PPI particles forms crystalline domains with an average of 8 stacked lamellae, compared to 10 for the larger particle systems. In contrast, pure CB had domains with an average of 13 lamellae at this time. However, in the β'-phase, the domain size is similar for all systems. This suggests that the PPI particles slightly hinder the growth of α-nuclei, and/or lead to the formation of a greater number of smaller crystals, potentially by acting as sites for heterogeneous nucleation.

3.3.2. *Effect of PPI particles on CB crystal morphology*

The microstructures of the different polymorphic forms of CB and CB + PPI particles were also imaged via polarised light (PLM) and optical (OM) microscopy. PLM showed crystal formation just prior to reaching 20 °C, in agreement with literature (Ladd Parada, 2018). After 20 min at 20 °C small crystals clustered to form a granular morphology with distinct regions containing very few crystals (Fig. 7a). Large particles are visible in the OM images of the CB with 18 μm PPI (Fig. 7d). Large dark regions were also observed in PLM images, which were believed to correspond to these large particles (indicated by the white circle in Fig. 7c). CB crystals in the presence of the larger protein particles appeared to be of smaller size and clusters (Fig. 7c). More crystals were observed in the visual field with smaller regions of no signal. The smaller PPI particles were observed in the OM images of the 3 μm particle blend (Fig. 7f), and PLM revealed a more homogeneous distribution of crystals, with smaller regions of no crystals (Fig. 7e). The more distinct crystal cluster domains observed in pure CB may be due to a lower number of larger crystal nuclei (Fig. 7a). The particle blends contain foreign (protein) particulate surfaces which may act as heterogeneous nucleation sites, reducing the free energy required for nucleation (Metin & Hartel, 2005). Such behaviour was observed by Yoshikawa et al. who reported that the addition of 1 wt% solid particles promoted the crystallisation of three monoacid saturated triacylglycerols. The additives had a range of hydrophobic and hydrophilic properties and initial crystallisation at the surface of the particles was confirmed using PLM (Yoshikawa et al., 2014).

After 7 days, new crystal morphologies had developed. Feather-like, dendritic spherulites were observed in all samples, some with granular centres (Fig. 8) in good agreement with literature (Marangoni & McGauley, 2003; Ladd Parada, 2018). Smaller spherulites with distinct coloured regions in a petal-like structure were also observed, with branches extending around the periphery (Fig. 8b). In samples containing either size of PPI particles, these large distinct coloured regions were smaller, indicating smaller crystalline domain sizes (Fig. 8d and h).

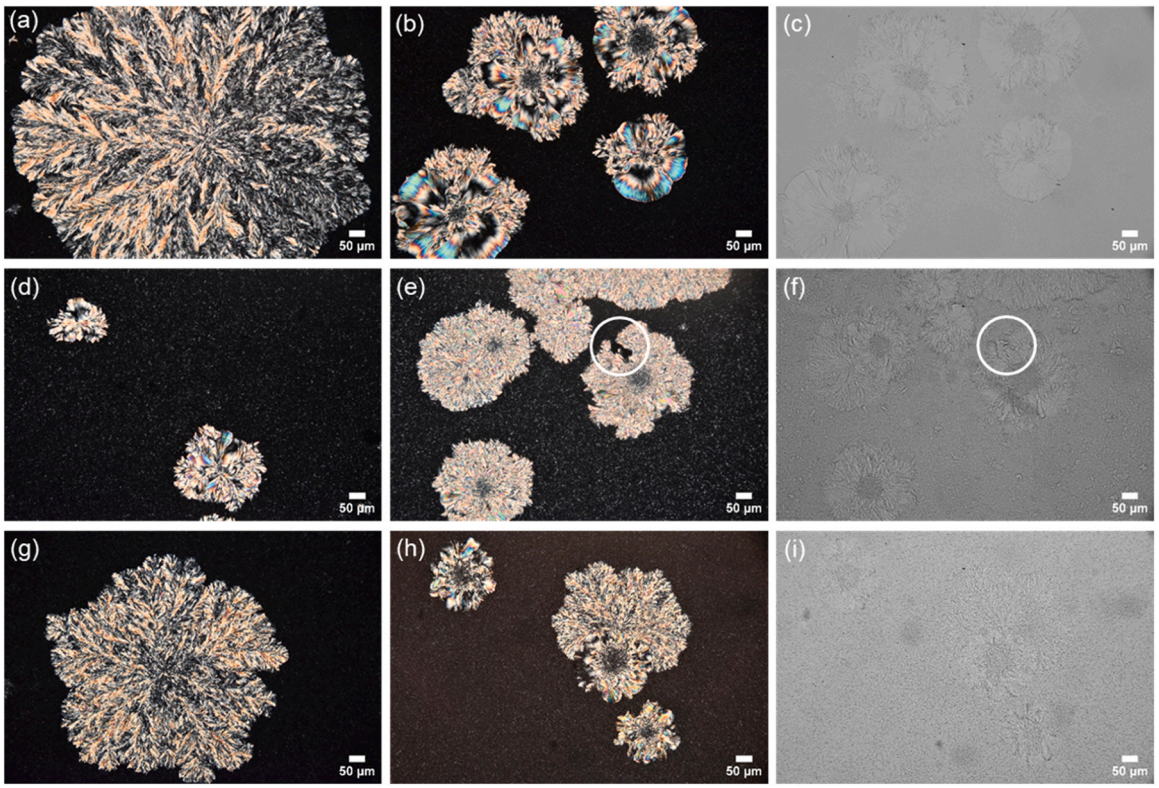

Fig. 8. PLM (a, b, d, e, g, h) and OM (c, f, i) images of (a-c) CB and CB with varying particle sizes of PPI at a concentration of 10 wt%, (d-f) 18 μm and (g-i) 3 μm crystallised at 20 °C for 7 days. White circles in (e) and (f) highlight crystal features around a larger PPI particle. All images were taken at 20x magnifcation and OM images were brightness adjusted to improve visibility.

In the sample with larger PPI particles, OM imaging revealed protein particles embedded both within and dispersed outside the larger crystal structures. White circles in Fig. 8e and f illustrate a larger spherulite growing around a large PPI particle, forming a discontinuity in the crystal structure.

3.3.3. *Effect of protein particles on CB crystallisation kinetics*

The crystallisation kinetics of CB and CB + milled PPI particles were examined by pulsed NMR, whereby the increase in solid fat content (SFC) was measured over time. The crystallisation curves for all samples during the first 120 min of isothermal conditions show a two-step process (Fig. 9a). This is associated with the sequential growth of the α- and β'-polymorphs which is consistent with the polymorphic transitions observed by X-ray scattering (Fig. 5). While PPI particles do not affect this transition pathway, differences in crystal growth kinetics were observed. The modified Gompertz model (Eq. 5) was applied to the data and the parameters of the second crystallisation event are shown in Figs. 9c and 9d. The addition of milled PPI particles lowered the induction time of the second CB crystallisation event (Fig. 9c) ($p < 0.05$). Protein particle size had minimal influence on the crystallisation kinetics; the 18 and 3 μm PPI systems displayed comparable crystallisation curves. Increasing the concentration of the larger PPI from 10 to 20 wt% led to a slight decrease in induction time, although this was within experimental error. All samples exhibited similar crystallisation rates ($p > 0.05$).

The effect of protein particles on the crystallisation induction time suggests that the particle surface could be acting as a heterogeneous nucleation site. Sugar and cocoa particles have been shown to accelerate CB nucleation and growth (Simoes et al., 2021; Svanberg et al., 2011). If surface effects alone governed behaviour, it would be expected that the CB system with the smaller 3 μm PPI would exhibit the fastest crystallisation. However, the crystallisation behaviour of this system was like that of the 18 μm particles. The 3 μm particle blend displayed an order of magnitude higher η at low shear rates compared to the 18 μm CB suspension (Fig. 3). This increase in η reduces molecular motion, limiting TAG diffusion and thus slowing crystallisation (Campos et al., 2010; Simoes et al., 2021; West & Rousseau, 2016). In the mixed CB + PPI systems, the interplay of these effects likely governs crystallisation kinetics; an increase in protein surface area accelerates nucleation, while an increase in viscosity hinders crystal growth. Given that the presence of protein particles accelerates the formation of solid fat relative to pure CB, it suggests surface effects dominate in these systems.

An increase in crystallisation rate and reduction in induction time is commonly attributed to the formation of a greater number of smaller crystals (Gregersen et al., 2015; Hubbes et al., 2020; Kalic et al., 2018). The influence of PPI particles on the crystallisation kinetics may therefore explain the observed reduction in crystalline domain size in the α-phase measured by X-ray scattering (Fig. 6b).

Although the 20 wt% larger PPI particles have a smaller overall particle surface area than 10 wt% 3 μm PPI, the crystallisation kinetics were similar. As the low shear viscosities of these two systems were also comparable (Fig. 3), this may be due to differences in the protein surface properties. The larger PPI particles may have more active sites for nucleation which are altered upon further milling down to 3 μm. Attempts to characterise the protein structure after milling via circular dichroism were unsuccessful due to the high absorbance of the oil phase (data not shown). Fig. 9b shows the SFC of CB and CB + PPI after 1 and 7 days. Although CB exhibited higher SFC after 1 day than CB + PPI samples ($p < 0.05$), the SFC values were comparable after 7 days ($p > 0.05$) suggesting no significant effect of PPI on SFC over extended storage conditions.

3.3.4. *Effect of protein particles on CB crystal network formation*

The crystallisation behaviour of the CB and CB + PPI particles was also studied using oscillatory rheology to monitor the temporal evolution of microstructure formed during isothermal crystallisation at 20 °C.

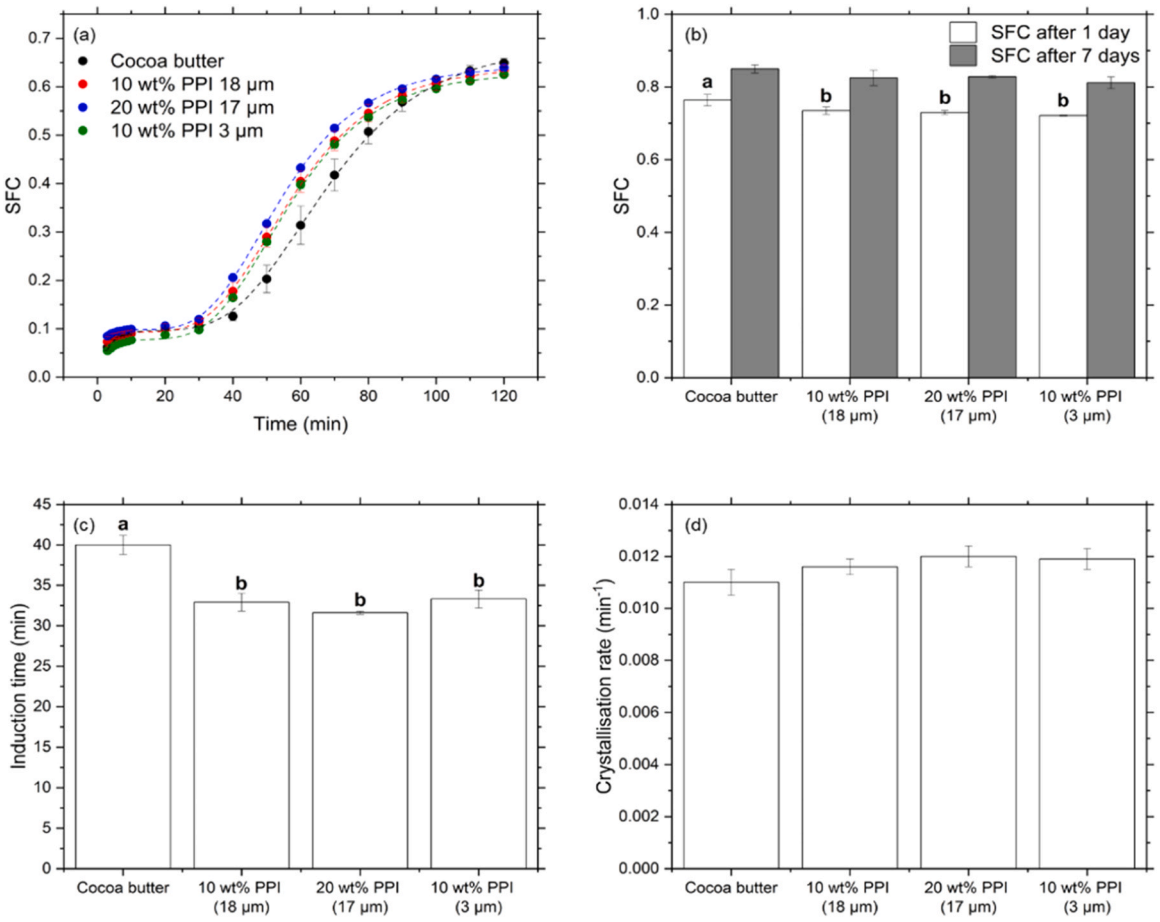

Fig. 9. Solid fat content (SFC) of CB and CB with varying sizes of PPI, crystallised at 20 °C. (a) SFC evolution over 120 min with dashed lines denoting the modified Gompertz model (Eq. 5): CB (black), 10 wt% PPI 18 μm (red), 20 wt% PPI 17 μm (blue), and 10 wt% PPI 3 μm (green). Corresponding R^2 values: for CB 0.997, for all the other systems 0.999. (b) SFC measured after 1 and 7 days. (c) Induction times and (d) crystallisation rates derived from the modified Gompertz model respectively. Different lower-case letters in the same bar chart indicate a statistically significant difference ($p < 0.05$).

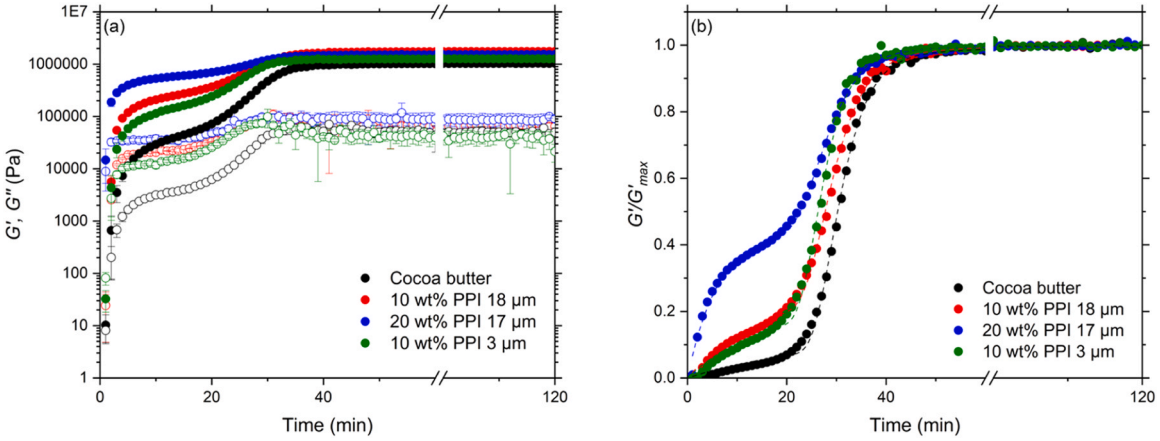

Fig. 10. (a) *G', G''* and (b) normalised storage modulus (G'/G'_{max}), as a function of time for CB and CB with varying sizes and concentrations of milled PPI during crystallisation at 20 °C: CB (black), 10 wt% PPI 18 μm (red), 20 wt% PPI 17 μm (blue), and 10 wt% PPI 3 μm (green). Dashed lines in (b) represent the fit to the modified Gompertz model (Eq. 5), adapted for $G'/G'_{max}(t)$. Corresponding R^2 values were all 0.999. Samples were subjected to a heating and cooling cycle prior to the isothermal hold.

Within a few min all samples exhibited gel-like behaviour ($G' > G''$), confirming that a very low SFC is sufficient to form a three-dimensional network (Fig. 10a). For fat crystallisation, this process occurs by simultaneous crystallisation and aggregation of fat crystals via van der Waals interactions to form clusters which associate into a network structure (De Graef et al., 2007; Narine & Marangoni, 1999). Like the pulsed NMR results, G' increases by a two-step process, attributed to the α to β' polymorphic transition. During the initial 20 min of crystallisation, G' of the milled PPI systems are an order of magnitude higher than that of pure CB.

Since the SFC of CB and CB + PPI particles was similar during the initial stages of crystallisation, the observed differences in viscoelasticity may be due to changes in fat crystal morphology in the presence of the PPI. The X-ray scattering and PLM indicated smaller fat crystal domains and clusters in the presence of PPI during the early stages of crystallisation. An increased number of smaller fat crystals would have a larger overall surface area, and therefore more fat crystal-fat crystal interactions per unit mass, promoting network formation. This effect has been observed in palm oil crystallised in the presence of sugar particles, where smaller fat crystals and higher elasticity were reported compared to pure palm oil (Hubbes et al., 2020; West & Rousseau, 2016). Hubbes et al. (2020) attributed this behaviour to sugar particles providing junction points between fat crystals during crystallisation, acting as active fillers within the network. Since the protein particles reduced the induction time of crystallisation, it is possible that the PPI particles act as heterogeneous nucleation sites. This may facilitate links between aggregating fat crystals in dilute conditions, strengthening the network and contributing to the observed increase in elasticity. It is thought that a combination of both mechanisms could give rise to the observed mechanical behaviour.

After the second crystallisation event, the elastic moduli of all networks reached an equilibrium value (G'_{max}) of the same order of magnitude. This likely due to the formation of a percolated network structure of fat crystals, owing to the high SFC of the samples. These results highlight the potential to replace solid fat with protein particles whilst maintaining the mechanical properties of a pure fat system. The relationship between normalised elastic modulus (G'/G'_{max}) and time during crystallisation provides information into the kinetics of the structure formation. The temporal evolution of the normalised values of G' were well described by the modified Gompertz model, with all R^2 values exceeding 0.99 (Fig. 10b). The same two-step model previously applied to SFC(t) (Eq. 5) was used here, with $G'/G'_{max}(t)$ substituted for SFC(t) and a new set of fit parameters obtained to describe the rheological data (Bölük et al., 2024). In agreement with pulsed NMR, the induction time of the second, large increase in G' is lower for the milled CB + PPI blends compared to pure CB (Figure S7). Although the trend is similar, the induction times deduced from pulsed NMR differ from those derived from the rheology data. This is likely due to the differences in sample volume between the two techniques. The addition of PPI particles also accelerates the approach to the equilibrium value of G'.

4. Conclusions

This study reports, for the first time, the influence of pea protein isolate (PPI) particles on the rheological and crystallisation behaviour of CB. The size of PPI particles *directly* dispersed in CB was successfully tuned by mechanical milling, achieving fine and coarse particle dispersions. The effect of these particles on the flow behaviour of molten CB was examined; as the size of the particles was reduced, the viscosity (η) and elasticity (G') of the systems increased. Networks of the smaller PPI particles also exhibited greater resistance to yielding.

Under isothermal crystallisation conditions, PPI particles had no effect on the crystal structure of CB, indicating that they are not integrated into the crystal lattice. The polymorphic transition was also unchanged in the presence of the particles. However, the crystal domain size during the initial period of crystallisation was found to be lower in the presence of PPI and microscopy also indicated a greater number of smaller crystal clusters in CB + PPI blends. Further examination into the crystallisation kinetics found that crystallisation was induced more rapidly in the presence of PPI, potentially via heterogeneous nucleation. This was thought to be the reason for the smaller crystalline domain size. Despite differences in nucleation behaviour, no significant effect of PPI on SFC during extended storage was observed.

At low SFC, PPI particles increased the elasticity of CB by an order of magnitude. However, as further crystallisation occurred, the elasticities of the blended systems were comparable to that of pure CB. Smaller fat crystals and clusters in the presence of PPI may give rise to the observed differences in viscoelasticity. This behaviour highlights the potential of PPI as a rheological modifier to alter texture and reduce solid fat content in confectionery applications.

CRediT authorship contribution statement

Isabel Celigueta Torres: Writing – review & editing, Supervision, Funding acquisition, Conceptualization. **Michael Rappolt:** Writing – review & editing, Visualization, Validation, Supervision, Methodology, Formal analysis. **Anwesha Sarkar:** Writing – review & editing, Supervision, Funding acquisition. **Brent Stuart Murray:** Writing – review & editing, Validation, Supervision, Project administration, Methodology, Funding acquisition, Conceptualization. **Evi Paximada:** Writing – review & editing. **Megan Holdstock:** Writing – review & editing, Writing – original draft, Visualization, Validation, Methodology, Investigation, Formal analysis, Data curation.

Declaration of Competing Interest

The authors declare that they have no conflicts of interest regarding this submission.

Acknowledgements

Authors gratefully acknowledge the Engineering and Physical Sciences Research Council (EPSRC) funded Centre for Doctoral Training in Soft Matter for Formulation and Industrial Innovation (SOFI2), Grant Ref. No. EP/S023631/1 as well as Nestlé PTC Confectionery (York, UK) for financial support. Authors BSM and AS acknowledge funding from the UK National Alternative Proteins Innovation Centre (NAPIC), funded by the Biotechnology and Biological Sciences Research Council (BBSRC) and Innovate UK (Grant Ref: BB/Z516119/1).

Appendix A. Supporting information

Supplementary data associated with this article can be found in the online version at doi:10.1016/j.foostr.2025.100476.

Data availability

Data will be made available on request.

References

Acevedo, N. C., & Marangoni, A. G. (2010). Toward nanoscale engineering of triacylglycerol crystal networks. *Crystal Growth and Design, 10*(8), 3334–3339. https://doi.org/10.1021/cg100469x

Bayés-García, L., Yoshikawa, S., Aguilar-Jiménez, M., Ishibashi, C., Ueno, S., & Calvet, T. (2022). Heterogeneous nucleation effects of talc particles on polymorphic crystallization of cocoa butter. *Crystal Growth and Design, 22*(1), 213–227. https://doi.org/10.1021/acs.cgd.1c00859

Beckett, S. T. (2009). Industrial chocolate manufacture and use: Fourth edition. *Industrial Chocolate Manufacture and Use: Fourth Edition*. https://doi.org/10.1002/9781444301588

Bölük, E., Akdeniz, E., Gunes, R., Palabiyik, I., Konar, N., & Toker, O. S. (2024). Determination of the process effect on cocoa butter crystallization by rheometer: Kinetic modeling by gompertz equation. *Journal of Food Science, 89*(5), 2867–2878. https://doi.org/10.1111/1750-3841.17040

Campos, R., Ollivon, M., & Marangoni, A. G. (2010). Molecular composition dynamics and structure of cocoa butter. *Crystal Growth and Design, 10*(1), 205–217. https://doi.org/10.1021/cg900853e

Chauhan, R. R., Dullens, R. P. A., Velikov, K. P., & Aarts, D. G. A. L. (2017). The effect of colloidal aggregates on fat crystal networks. *Food and Function, 8*(1), 352–359. https://doi.org/10.1039/c6fo01622g

Co, E. D., & Marangoni, A. G. (2019). Colloidal networks of fat crystals. *Advances in Colloid and Interface Science, 273*, Article 102035. https://doi.org/10.1016/j.cis.2019.102035

De Graef, V., Foubert, I., Smith, K. W., Cain, F. W., & Dewettinck, K. (2007). Crystallization behavior and texture of trans-containing and trans-free palm oil based confectionery fats. *Journal of Agricultural and Food Chemistry, 55*(25). https://doi.org/10.1021/jf071967q

De Vries, A., Hendriks, J., Van Der Linden, E., & Scholten, E. (2015). Protein oleogels from protein hydrogels via a stepwise solvent exchange route. *Langmuir, 31*(51), 13850–13859. https://doi.org/10.1021/acs.langmuir.5b03993

Feichtinger, A., Nibbelink, D. G., Poppe, S., Bozzo, L., Landman, J., & Scholten, E. (2022). Protein oleogels prepared by solvent transfer method with varying protein sources. *Food Hydrocolloids, 132*, Article 107821. https://doi.org/10.1016/j.foodhyd.2022.107821

Feichtinger, A., Scholten, E., & Sala, G. (2020). Effect of particle size distribution on rheological properties of chocolate. *Food and Function, 11*(11), 9547–9559. https://doi.org/10.1039/d0fo01655a

Firestone, D. (1998). *Official methods and recommended practices of the American oil Chemists' society*. AOC Press.

Foubert, I., Dewettinck, K., Janssen, G., & Vanrolleghem, P. A. (2006). Modelling two-step isothermal fat crystallization. *Journal of Food Engineering, 75*(4), 551–559. https://doi.org/10.1016/j.jfoodeng.2005.04.038

Gregersen, S. B., Miller, R. L., Hammershøj, M., Andersen, M. D., & Wiking, L. (2015). Texture and microstructure of cocoa butter replacers: Influence of composition and cooling rate. *Food Structure, 4*, 2–15. https://doi.org/10.1016/j.foostr.2015.03.001

Gribnau, M. C. M. (1992). Determination of solid/liquid ratios of fats and oils by low-resolution pulsed NMR. *Trends in Food Science and Technology, 3*(C). https://doi.org/10.1016/0924-2244(92)90187-2

He, K., Chen, N., Wang, C., Wei, L., & Chen, J. (2018). Method for determining crystal grain size by X-Ray diffraction. *Crystal Research and Technology, 53*(2). https://doi.org/10.1002/crat.201700157

Holdstock, M., Murray, B. S., Sarkar, A., Paximada, P., Rappolt, M., & Celigueta Torres, I. (2025). Dispersion behaviour of insoluble particles with different surface properties in non-aqueous media – biopolymer based oleogels. *Soft Matter, 21*, 7460–7475. https://doi.org/10.1039/D5SM00596E

Hubbes, S. S., Braun, A., & Foerst, P. (2020). Sugar particles and their role in crystallization kinetics and structural properties in fats used for nougat creme production. *Journal of Food Engineering, 287*, Article 110130. https://doi.org/10.1016/j.jfoodeng.2020.110130

Kalic, M., Krstonosic, V., Hadnadev, M., Gregersen, S. B., Jovanovic Ljeskovic, N., & Wiking, L. (2018). Impact of different sugar and cocoa powder particle sizes on crystallization of fat used for the production of confectionery products: Particle size distribution influences fat crystallization. *Journal of Food Processing and Preservation, 42*(12), Article e13848. https://doi.org/10.1111/jfpp.13848

Ladd Parada, M. (2018). The effects of pressure and thermal history on the crystallisation of cocoa butter [PhD, University of Leeds]. ⟨https://etheses.whiterose.ac.uk/id/eprint/22114/⟩.

Li, C., McClements, D. J., Dai, T., Deng, L., Feng, Z., Li, T., Liu, C., & Chen, J. (2023). Enhancing the dispersibility of commercial pea protein ingredients using stirred media milling: Potential mechanisms of action. *Food Hydrocolloids, 145*, Article 109130. https://doi.org/10.1016/j.foodhyd.2023.109130

Marangoni, A. G., & McGauley, S. E. (2003). Relationship between crystallization behavior and structure in cocoa butter. *Crystal Growth and Design, 3*(1), 95–108. https://doi.org/10.1021/cg025580l

Marangoni, A. G., & Rousseau, D. (1996). Is plastic fat rheology governed by the fractal nature of the fat crystal network? *JAOCS, Journal of the American Oil Chemists' Society, 73*(8), 991–994. https://doi.org/10.1007/BF02523406

Metin, S., & Hartel, R. W. (2005). Crystallization of fats and oils. In F. Shahidi (Ed.) (6th ed.,*Bailey's Industrial Oil and Fat Products* (6th ed.,*, 1* pp. 45–76). John Wiley & Sons. https://doi.org/10.1002/047167849x.bio021.

Narine, S. S., & Marangoni, A. G. (1999). Relating structure of fat crystal networks to mechanical properties: A review. *Food Research International, 32*(4), 227–248. https://doi.org/10.1016/S0963-9969(99)00078-2

Plazzotta, S., Calligaris, S., & Manzocco, L. (2020). Structural characterization of oleogels from whey protein aerogel particles. *Food Research International, 132*, Article 109099. https://doi.org/10.1016/j.foodres.2020.109099

Pratama, Y., Burholt, S., Baker, D. L., Sadeghpour, A., Simone, E., & Rappolt, M. (2022). Polymorphism of a highly asymmetrical triacylglycerol in milk fat: 1-Butyryl 2-Stearoyl 3-Palmitoyl-glycerol. *Crystal Growth and Design, 22*(10), 6120–6130. https://doi.org/10.1021/acs.cgd.2c00713

Romoscanu, A. I., & Mezzenga, R. (2006). Emulsion-templated fully reversible protein-in-oil gels. *Langmuir, 22*(18), 7812–7818. https://doi.org/10.1021/la060878p

Sarkar, A., Arfsten, J., Golay, P. A., Acquistapace, S., & Heinrich, E. (2016). Microstructure and long-term stability of spray dried emulsions with ultra-high oil content. *Food Hydrocolloids, 52*, 857–867. https://doi.org/10.1016/j.foodhyd.2015.09.003

Shewan, H. M., Deshmukh, O. S., Chen, G., Rodrigues, S., Selway, N., & Stokes, J. R. (2021). Interpreting rheological behaviour of sugar-fat mixtures as a function of solids phase volume. *Journal of Food Engineering, 297*, Article 110474. https://doi.org/10.1016/j.jfoodeng.2020.110474

Simoes, S., Lelaj, E., & Rousseau, D. (2021). The presence of crystalline sugar limits the influence of emulsifiers on cocoa butter crystallization. *Food Chemistry, 346*, Article 128848. https://doi.org/10.1016/j.foodchem.2020.128848

Simone, E., Rappolt, M., Ewens, H., Rutherford, T., Marty Terrade, S., Giuffrida, F., & Marmet, C. (2024). A synchrotron X-ray scattering study of the crystallization behavior of mixtures of confectionary triacylglycerides: Effect of chemical composition and shear on polymorphism and kinetics. *Food Research International, 177*, Article 113864. https://doi.org/10.1016/j.foodres.2023.113864

Svanberg, L., Ahrné, L., Lorén, N., & Windhab, E. (2011). Effect of sugar, cocoa particles and lecithin on cocoa butter crystallisation in seeded and non-seeded chocolate model systems. *Journal of Food Engineering, 104*(1), 70–80. https://doi.org/10.1016/j.jfoodeng.2010.09.023

de Vries, A., Wesseling, A., van der Linden, E., & Scholten, E. (2017). Protein oleogels from heat-set whey protein aggregates. *Journal of Colloid and Interface Science, 486*, 75–83. https://doi.org/10.1016/j.jcis.2016.09.043

West, R., & Rousseau, D. (2016). Crystallization and rheology of palm oil in the presence of sugar. *Food Research International, 85*, 224–234. https://doi.org/10.1016/j.foodres.2016.05.010

West, R., & Rousseau, D. (2017). Modelling sugar, processing, and storage effects on palm oil crystallization and rheology. *LWT, 83*, 201–212. https://doi.org/10.1016/j.lwt.2017.05.021

Yoshikawa, S., Kida, H., Matsumura, Y., & Sato, K. (2016). Adding talc particles improves physical properties of palm oil-based shortening. *European Journal of Lipid Science and Technology, 118*(7), 1007–1017. https://doi.org/10.1002/ejlt.201500283

Yoshikawa, S., Kida, H., & Sato, K. (2014). Promotional effects of new types of additives on fat crystallization. *Journal of Oleo Science, 63*(4), 333–345. https://doi.org/10.5650/jos.ess13155

Zhang, Z., Zhou, F., & Lavernia, E. J. (2003). On the analysis of grain size in bulk nanocrystalline materials via x-ray diffraction. *Metallurgical and Materials Transactions A, 34*(A(6)), 1349–1355. https://doi.org/10.1007/s11661-003-0246-2